RSC Advances

PAPER

Cite this: *RSC Adv.*, 2025, **15**, 30217

Visible light-driven photocatalytic degradation of rhodamine B and 5-fluorouracil using ZIF-8/GO: unveiling mechanisms

Iqra Rabani,[a] Nguyen Tien Tran,[bc] Muhammad Faheem Maqsood,[d]
Mosab Kaseem,[e] Ghulam Dastgeer[f] and Hai Bang Truong *[gh]

Received 18th July 2025
Accepted 19th August 2025

DOI: 10.1039/d5ra05177k

rsc.li/rsc-advances

The removal of pharmaceutical and organic contaminants from wastewater remains a pressing challenge for conventional treatment technologies. In this study, a novel photocatalyst composed of Zeolitic Imidazolate Framework-8 (ZIF-8) nanocrystals integrated with a graphene oxide (GO) matrix was developed *via* a facile interfacial synthesis approach. The structural and morphological properties of the resulting ZIF-8/GO composite were characterized using X-ray diffraction, X-ray photoelectron spectroscopy, and transmission electron microscopy. The composite's photocatalytic efficiency was assessed through the degradation of Rhodamine B (Rho-B), a representative dye pollutant, and 5-fluorouracil (5-Flu), a widely used pharmaceutical, under visible light irradiation. The ZIF-8/GO catalyst achieved near-complete degradation of Rho-B (100%) and 5-Flu (97.4%) within 100 minutes. This high performance is attributed to the synergistic effects of ZIF-8 and GO, which enhance surface area, improve light absorption, and promote charge separation. Moreover, the catalyst retained considerable activity over five cycles, with only a 12.8% decrease in Rho-B degradation due to minor material loss. The findings demonstrate that the ZIF-8/GO composite is a highly efficient, recyclable, and sustainable photocatalyst, showing great promise for the removal of complex pollutants from wastewater and contributing to environmentally friendly water purification technologies.

1. Introduction

Organic dyes are substantial environmental pollutants, often released into water bodies through industrial processes including printing, dyeing and textile manufacturing.[1–3] Globally, it is estimated that over 700 000 tons of dyes are produced annually, and approximately 10–15% of these enter aquatic systems as waste, contributing significantly to water pollution. These dyes are not only aesthetically unappealing but also pose serious environmental hazards due to their potential carcinogenicity, toxicity, and resistance to biodegradation.[4,5] Conventional wastewater treatment processes frequently fail to entirely eliminate these dyes, leading to their determination in groundwater, surface water and even drinking water supplies.[6,7] This ongoing contamination poses risks to aquatic life and human health, highlighting the urgent need for advanced treatment methods.[8]

In addition to dye pollution, pharmaceutical pollutants—particularly anticancer drugs—have become emerging contaminants of global concern.[9,10] Studies indicate that the worldwide consumption of anticancer drugs exceeds 75 tons per year, with a considerable fraction excreted unmetabolized into sewage systems.[11–15] Significant research efforts have shown that anticancer pharmaceuticals, even at trace concentrations in the ng L^{-1} to μg L^{-1} range, exert cytotoxic effects on aquatic organisms, including impaired reproduction, growth inhibition, and genotoxicity.[16,17] Although these drugs are formulated to disrupt RNA or DNA synthesis in malignant cells, their stability and toxicity render them hazardous to aquatic ecosystems.[18] Consequently, there is an urgent need to develop efficient strategies for eliminating anticancer agents from water bodies. These compounds, aimed at inhibiting cellular proliferation, are typically resistant to biodegradation and poorly removed by conventional biological treatment processes.[19]

---

[a] *Antwerp Engineering, Photoelectrochemistry and Sensing (A-PECS), University of Antwerp, Groenenborgerlaan 171, 2020 Antwerp, Belgium*
[b] *Center for Advanced Chemistry, Institute of Research and Development, Duy Tan University, 03 Quang Trung, Da Nang 550000, Vietnam*
[c] *Faculty of Natural Sciences, Duy Tan University, 03 Quang Trung, Da Nang 550000, Vietnam*
[d] *School of Engineering, The Australian National University, Canberra, Australian Capital Territory, 2601, Australia*
[e] *Department of Nanotechnology and Advanced Materials Engineering, Sejong University, Seoul 05006, Republic of Korea*
[f] *Department of Physics and Astronomy, Sejong University, Seoul 05006, South Korea*
[g] *Optical Materials Research Group, Science and Technology Advanced Institute, Van Lang University, Ho Chi Minh City, Vietnam*
[h] *Faculty of Applied Technology, Van Lang School of Technology, Van Lang University, Ho Chi Minh City, Vietnam. E-mail: truonghaibang@vlu.edu.vn*

Advanced oxidation processes (AOPs) have emerged as a viable alternative for degrading such contaminants, leveraging reactive species to break down pollutants.[20–22] A wide range of AOPs, including ozonation, UV/chlorine, photo-Fenton, sonolysis, wet oxidation, and photocatalysis, as well as integrated hybrid approaches, have been employed to degrade organic contaminants.[23–28] Among these, photocatalysis is predictable as eco-friendly remediation methods, garnering significant attention.[1,29–31] This technique has been employed to degrade the organic pollutants from wastewater by producing highly reactive chemical species that can mineralize a wide range of organic contaminants.[32] However, conventional photocatalysts often exhibit drawbacks such as broad bandgaps and limited surface areas, which hinder their practical efficiency in water treatment applications.[8,30,33] These drawbacks necessitate the development of advanced photocatalytic materials that can overcome these challenges and provide enhanced performance in the degradation of both pharmaceutical and organic pollutants.

In this context, metal–organic frameworks (MOFs) have emerged as a class of crystalline porous materials composed of metal clusters coordinated with organic ligands.[4,34] By carefully selecting organic and inorganic components, MOFs can be engineered to have specific properties and architectures.[35] In recent years, MOFs have emerged as versatile materials with different implementations, including drug delivery gas capture and separation technologies, as well as light-driven catalytic processes.[36–38] A subclass of MOFs, Zeolitic Imidazole Frameworks (ZIFs), such as ZIF-8, consists of organic linkers and coordinated inorganic clusters. ZIF-8 is particularly notable for its ability to act as both a sacrificial template and a metal precursor.[39,40] Its attributes, such as a high surface area, adjustable porosity, and superior chemical durability, (with pore sizes around 1.16 nm and a pore volume of 0.60 $cm^3\ g^{-1}$), make ZIF-8 especially attractive for applications in photocatalysis.[41–43]

Specifically, ZIF-8 has been employed for drug delivery in the treatment of cancer and bacterial infections. However, ZIF-8 has limitations, including poor light absorption, rapid recombination of photogenerated electron–hole pairs, and excessive release of Zn^{2+}, which can lead to reduced photocatalytic performance and cytotoxicity.[44] Forming composites with other materials has been a promising solution to these issues. In this regard, certain two-dimensional materials like GO,[45] $Ti_3C_2T_x$[46] and MoS_2 nanosheets[47] have demonstrated excellent photocatalytic properties. These materials can form heterojunctions with semiconductors, effectively tuning their bandgaps and thereby enhancing their photocatalytic performance.

Based on the versatile features of GO and ZIF-8, they are ideal candidates to combine using a cost-effective solvothermal strategy, making them effective photocatalysts. The synergistic effect between GO and ZIF-8 contributes to the formation of a well-defined, uniform composite structure with enhanced surface area, leading to improved charge separation. This study aims to: (1) synthesize a homogeneous ZIF-8 layer on a GO substrate to attain high surface area and porosity, (2) assess the photocatalytic performance of ZIF-8@GO utilizing dye (Rho-B) and drug (5-Flu) as model contaminants, (3) examine the influence of operational parameters on photocatalytic activity, (4) test the reusability and stability of the composite over five consecutive cycles, and (5) elucidate the degradation pathways of Rho-B and 5-Flu.

2. Experimental sections

2.1. Synthesis of the ZIF-8 on the matrix of GO

First, 9.88 mmol of $Zn(NO_3)_2\cdot 6H_2O$ was dissolved in 200 mL of methanol (MeOH), and 79.04 mmol of 2-MIM was dissolved in another 200 mL of MeOH. Separately, 200 mg of GO was dissolved in 40 mL of DMF to create a dispersion with a concentration of 5 mg mL^{-1}. This dispersion was then diluted with MeOH to achieve a concentration of 1 mg mL^{-1}. The zinc nitrate solution and GO dispersion were quickly added to the imidazole solution and stirred for 1 h, resulting in the formation of white crystals of ZIF-8 on GO at 25 °C. Thereafter, the mixture was centrifuged and washed with MeOH 2–3 times. Finally, the product was dried at 100 °C for approximately 24 h and labeled the product by ZIF-8/GO (Scheme 1).

2.2. Photocatalysis activity

Photocatalytic performance was evaluated using a photoreactor fitted with twelve 6 W visible-light LED lamps ($\lambda = 420$–700 nm, Philips). The reactor vessel was positioned at a distance of approximately 10 cm beneath the light source, delivering an estimated irradiance of 48 mW cm^{-2} at that location. In each run, 50 mg of the photocatalyst was introduced into a prepared solution containing 5-Flu (1 mg L^{-1}) and Rho-B (5 mg L^{-1}). All photocatalytic assays were conducted under identical initial conditions to ensure consistency and allow for reliable comparison across trials. Prior to illumination, the suspension containing the catalyst was magnetically stirred in the dark for 30 minutes to achieve adsorption–desorption equilibrium between the photocatalysts and the target pollutants. Visible light exposure was initiated, and aliquots were withdrawn at designated time intervals. Each sample was immediately filtered using a 0.45 μm PTFE syringe filter to eliminate any suspended catalyst particles. This step enabled accurate determination of the remaining concentrations of Rho-B and 5-Flu in solution. As a reference, a photolysis experiment was carried out under the same conditions but without the addition of catalyst, to assess the extent of direct photodegradation. The absorbance of the target compounds was measured at their characteristic maximum wavelengths using a UV-vis spectrophotometer.

To assess the durability and reuse potential of the catalyst, the used material was recovered, thoroughly rinsed with deionized water about five times, and reused in subsequent experiments. Additionally, to elucidate the role of reactive oxygen species (ROS) in the degradation mechanism, trapping experiments were performed. These tests involved adding specific scavengers to the reaction mixture to quench different ROS. Furfuryl alcohol (FFA) was used to quench hydroxyl radicals ($^{\bullet}OH$), *p*-benzoquinone (BQ) was used to quench superoxide radicals ($^{\bullet}O_2^{-}$), and ethylenediaminetetraacetic acid disodium

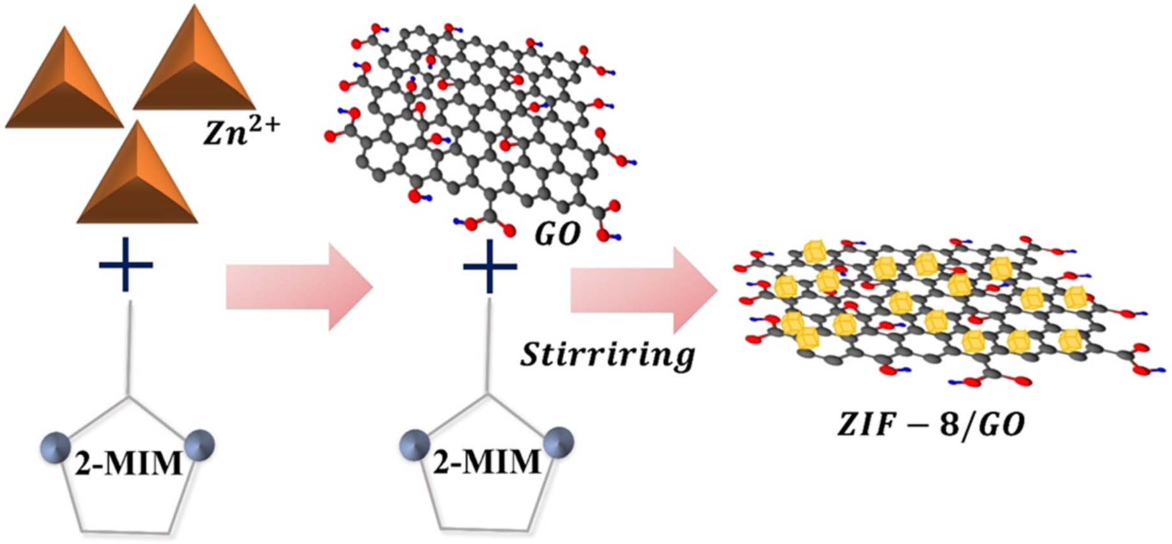

Scheme 1 Synthesis illustration of the ZIF-8 nanocrystals on GO matrix.

salt (EDTA-2Na) was used to quench photogenerated holes (h^+). By introducing these scavengers and monitoring the changes in the degradation rate, the contribution of each type of reactive species to the photocatalytic process could be determined. This approach helps to understand which ROS are most active in the degradation mechanism.

2.3. Material characterizations

The morphological characteristics and internal structure of the GO, ZIF-8 and ZIF-8/GO were analyzed using a JEM-2010 high-resolution transmission electron microscopy (HR-TEM). Elemental mapping was also conducted to determine the spatial distribution of elements. The crystal structure of the synthesized catalysts was characterized by powder X-ray diffraction (XRD) using a Panalytical XRD-6100 instrument (Panalytical, Malvern, UK). XRD data were collected in the 2θ range of 10°–80° at a scan speed of 5° min^{-1} with Cu Kα radiation ($\lambda = 1.5406$ Å). To assess the surface characteristics and porosity, nitrogen adsorption–desorption measurements were performed using a Micromeritics ASAP 2020 analyzer (Micromeritics Instrument Corp., Norcross, GA, USA). Additionally, X-ray photoelectron spectroscopy (XPS) was performed using a Thermo Scientific K-Alpha + XPS system to analyze the surface chemical states and elemental compositions of the catalysts.

3. Results and discussions

3.1. Analysis of structure and morphology

The morphology of GO, ZIF-8, and the ZIF-8/GO catalysts was investigated using TEM and FESEM. The TEM micrographs, presented in Fig. S1(a), provide detailed morphological information on these materials. It displays the TEM image of pristine GO, where the intersecting, nanoscale flake-like structures are clearly visible. These features are characteristic of GO's layered structure, which is essential for its functionality in composite materials. Fig. S1(b and c) show the FESEM micrographs of ZIF-8 at both high and low magnifications, highlighting its well-known rhombic dodecahedron morphology. This polyhedral shape is a hallmark of ZIF-8 crystals, reflecting their highly ordered and uniform crystal lattice.[39] The ZIF-8 particles are evenly distributed throughout the sample, forming a densely packed, highly ordered array.[10] The uniformity and consistency of the crystal shapes, even over large areas, underscore the successful synthesis and crystallization process. The TEM images in Fig. 1(a–c) depict the morphology of the ZIF-8/GO composite at high and low magnifications. The ZIF-8 particles, retaining their rhombic dodecahedron geometry, are uniformly dispersed across the GO sheets. This indicates a strong interaction between ZIF-8 and GO, where the ZIF-8 particles are effectively anchored onto the GO surface. The composite material benefits from the combination of GO's flexible, conductive matrix and ZIF-8's porous crystalline structure. The GO sheets provide mechanical strength and electrical conductivity, while the ZIF-8 crystals contribute significant surface area and adsorption capacity due to their porous nature.

To further assess the crystal distribution within the ZIF-8/GO composite catalyst, elemental mapping was conducted, with the results shown in Fig. 1(d–h). The analysis confirms a homogeneous distribution of elements throughout the composite, indicating a successful integration of the materials. This uniform dispersion contributes to enhanced functional properties. The interaction between the GO matrix and ZIF-8 particles results in a composite with superior performance characteristics, making it well-suited for high-value photocatalytic applications. Additionally, the EDS spectrum in Fig. 1(i) shows elemental peaks for carbon (C) and oxygen (O) from GO, along with zinc (Zn) and nitrogen (N) from ZIF-8, confirming the successful synthesis and integration of GO and ZIF-8 in the composite.

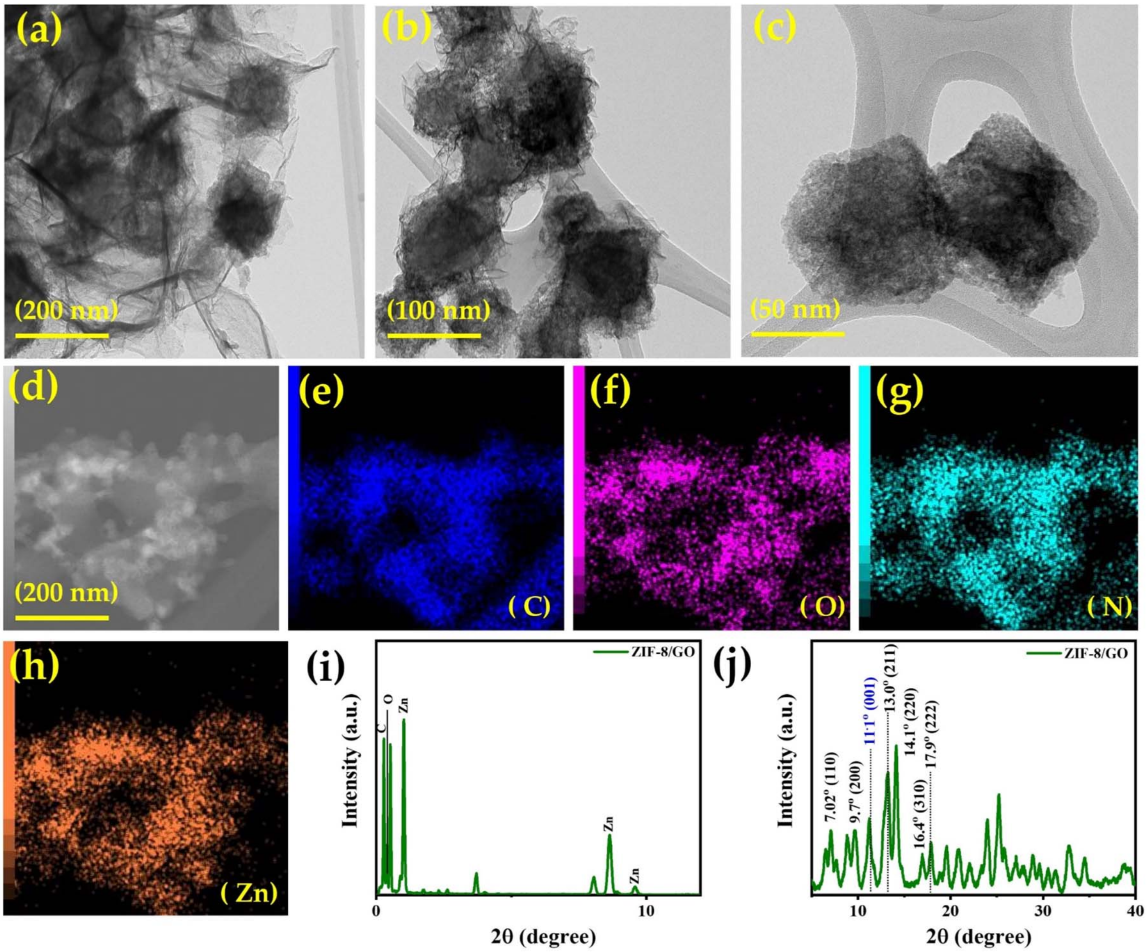

Fig. 1 TEM micrographs of (a–c) ZIF-8/GO composite at 200, 100 and 50 nm of magnifications, (d) ZIF-8/GO FESEM image for EdX, (e–h) EdX elemental mapping; C, O, N, Zn, respectively and (i and j) EDX plots and XRD pattern of the ZIF-8/GO composite.

To further examine the crystal structure, XRD analysis of the GO, ZIF-8, and the ZIF-8/GO composite was performed, with the resulting patterns shown in Fig. 1(j). Pristine GO (Fig. S2) displayed a prominent peak at a 2θ angle of 11.1°, which corresponds to the (001) plane.[48] This peak reflects the interlayer spacing between GO sheets and confirms the presence of oxygen-containing functional groups. Fig. S3 presents the XRD pattern for pristine ZIF-8 nanocrystals. ZIF-8 typically exhibits diffraction peaks at 7.02°, 10.2°, 12.6°, 14.6°, 16.4°, and 17.9°, which are consistent with the reported crystallographic data for this framework.[8,45] The XRD pattern of the ZIF-8/GO composite (Fig. 1(j)) shows diffraction peaks at 7.02°, 9.7°, 11.1°, 13.0°, 14.1°, 16.4°, and 17.9°, confirming the preservation of the crystalline structure of ZIF-8 within the composite. Importantly, the GO peak at 11.1° remains visible in the composite, although with a slight change in sharpness compared to pristine GO. This observation suggests that while ZIF-8 nanocrystals are successfully integrated with the GO sheets, the layered structure of GO is still partially retained. Minor shifts in some ZIF-8 peaks further indicate interactions between the two components, leading to subtle distortions in the crystal lattice.

To further investigate the surface features, BET measurements were carried out to measure the photocatalysts' specific surface area, with the results illustrated in Fig. 2(a and b). The N_2 adsorption/desorption isotherms of all catalysts show similar hysteresis loops, indicating comparable porosity, as depicted in Fig. 2(a and b). According to IUPAC classification, all catalysts exhibit type-I isotherms, suggesting strong interactions between the adsorbent and adsorbate.[49,50] However, GO demonstrates a type-IV isotherm with an H_3-type hysteresis loop under the same conditions,[51] as shown in Fig. 2(a). Based on the calculations of the BET measurements, the ZIF-8/GO composite showed highest surface area (2230 $m^2\ g^{-1}$), exceeding those of GO (720 $m^2\ g^{-1}$) and ZIF-8 (1190 $m^2\ g^{-1}$). In addition, BJH calculations revealed pore sizes of 1.134 nm (GO), 1.0134 nm (ZIF-8), and 0.6434 nm (ZIF-8/GO). Corresponding pore volumes were calculated as 0.026, 0.204, and 0.328 $cm^3\ g^{-1}$. The superior photocatalytic efficiency of the ZIF-8/GO composite is due to its larger surface area and mesoporsity, which promote efficient electron–hole pair separation. Thus, ZIF-8/GO composite was chosen as the optimized photocatalyst for further studies due to its high surface-to-volume ratio.

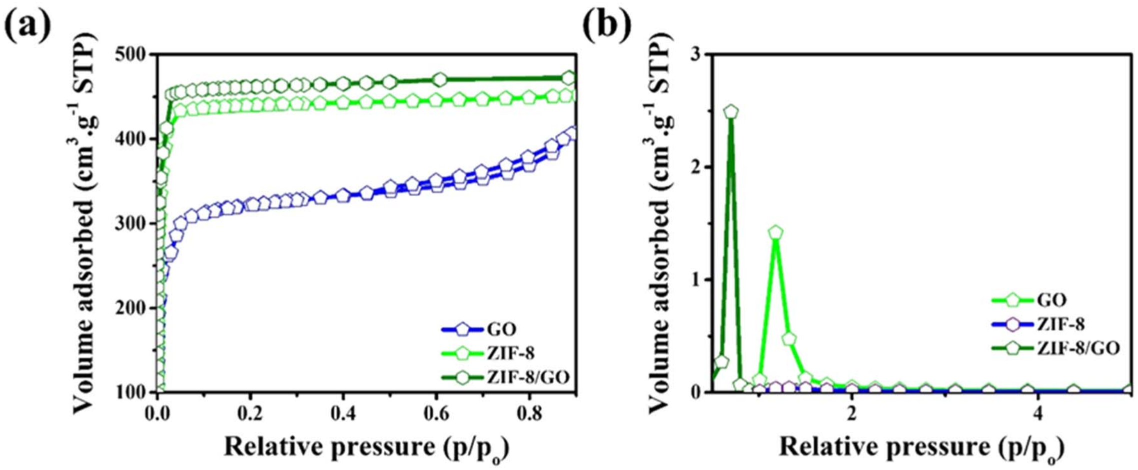

Fig. 2 BET analysis including (a and b) isothermal and BJH profiles for GO, ZIF-8 and ZIF-8/GO composite.

High-resolution XPS analysis was conducted to confirm the chemical composition and valence states of GO, ZIF-8, and the ZIF-8/GO composite, with results shown in Fig. 3. The ZIF-8/GO composite primarily consists of C, O, N, and Zn elements. In the C 1s spectrum of GO (Fig. 3(a)), peaks corresponding to various carbon–oxygen bonds were identified: C–C (sp^2 carbon) at 284.5 eV, O–C=O at 289 eV and C–O at 286.5 eV. ZIF-8 (Fig. 3(b)) showed peaks at 284.5 eV for C–C, 285.6 eV for C–N, and 287.8 eV for C=O.[34,52] The GO@ZIF-8 composite (Fig. 3(c)) exhibited peaks from both GO and ZIF-8, with slight shifts in XPS peaks attributed to synthesis conditions and crystal structure distortions.

The N 1s spectra for GO, ZIF-8, and the ZIF-8/GO composite reveal nitrogen-containing functional groups, with deconvolution showing Pyridinic N, Pyrrolic N, and Graphitic N peaks, corresponding to different chemical environments[4,53] (Fig. 3(d–f)). These nitrogen species influence the material's electronic structure and energy storage potential. The high-resolution Zn 2p XPS profiles for ZIF-8 and ZIF-8/GO (Fig. 3(g and h)) display Zn 2p3/2 at 1045.1 eV and Zn 2p1/2 at 1021.8 eV, indicating Zn^{2+} ions within the ZIF-8 framework, verifying the effective integration of ZIF-8 into the GO matrix.[54] The peak separation observed in the Zn 2p XPS spectra was 22.9 eV for ZIF-8 and slightly increased to 23.09 eV for the ZIF-8/GO composite. This small shift in peak separation suggests subtle changes in the electronic environment of the Zn^{2+} ions, likely due to the interaction between ZIF-8 and the GO matrix during composite formation.

3.2. Photodegradation of Rho-B

Photocatalytic activity offers a sustainable and effective approach to tackling various environmental issues, making it a significant technology in efforts to protect and improve the environment. In particular, it is valuable in water treatment and degrade organic pollutants, such as pharmaceuticals and industrial chemicals, which are challenging to remove with conventional methods.[55,56] This makes it a promising technology for purifying drinking water and wastewater. For this reason, the photocatalytic performance of GO, ZIF-8, and the ZIF-8/GO composite under visible light irradiation was evaluated using Rho-B as a model pollutant to assess their efficiency in photocatalytic degradation. All the prepared catalysts are tested to determine their ability to facilitate the degradation of Rho-B under visible light irradiation.

Initially, the photocatalytic performance of GO and ZIF-8 alone was assessed to establish a baseline for comparison. To assess the effect of light alone, the degradation of Rho-B was also monitored under visible light for 30 minutes without adding any photocatalyst. As shown in Fig. 4(a), the absorbance spectrum exhibited negligible change, indicating that Rho-B remained stable and did not undergo photodegradation in the absence of a photocatalyst.

To further investigate the adsorption–desorption equilibrium, experiments were conducted in the dark for 30 min using GO, ZIF-8 and ZIF-8/GO catalysts. The results, depicted in Fig. S4–S6, show that the absorbance intensity of Rho- B remained stable with GO and ZIF-8/GO catalysts, indicating no adsorption or desorption of the dye on these materials. In contrast, slight degradation of the absorbance spectra was observed with the ZIF-8, suggesting some level of interaction with the dye.

The absorbance intensity of Rho-B with GO showed a similar pattern when exposed to visible light for the 40 min, followed by a gradual decline over the next 100 min at the given interval, as illustrated in Fig. 4(b). This indicates that GO facilitates the photocatalytic degradation of Rho-B, but slowly. In the case of ZIF-8, a similar behavior was observed where the absorbance intensity of Rho-B decreased steadily under visible light for 100 min, as shown in Fig. 4(c). This suggests that ZIF-8 also contributes to the photocatalytic degradation of Rho-B, though at a consistent rate over time.

Upon introducing the ZIF-8/GO photocatalyst, a pronounced and continuous decline in the absorbance intensity of Rho-B was recorded from the onset of visible light irradiation up to 100 min, as seen in Fig. 4(d). This significant and sustained decrease indicates that the ZIF-8/GO catalyst possess enhanced

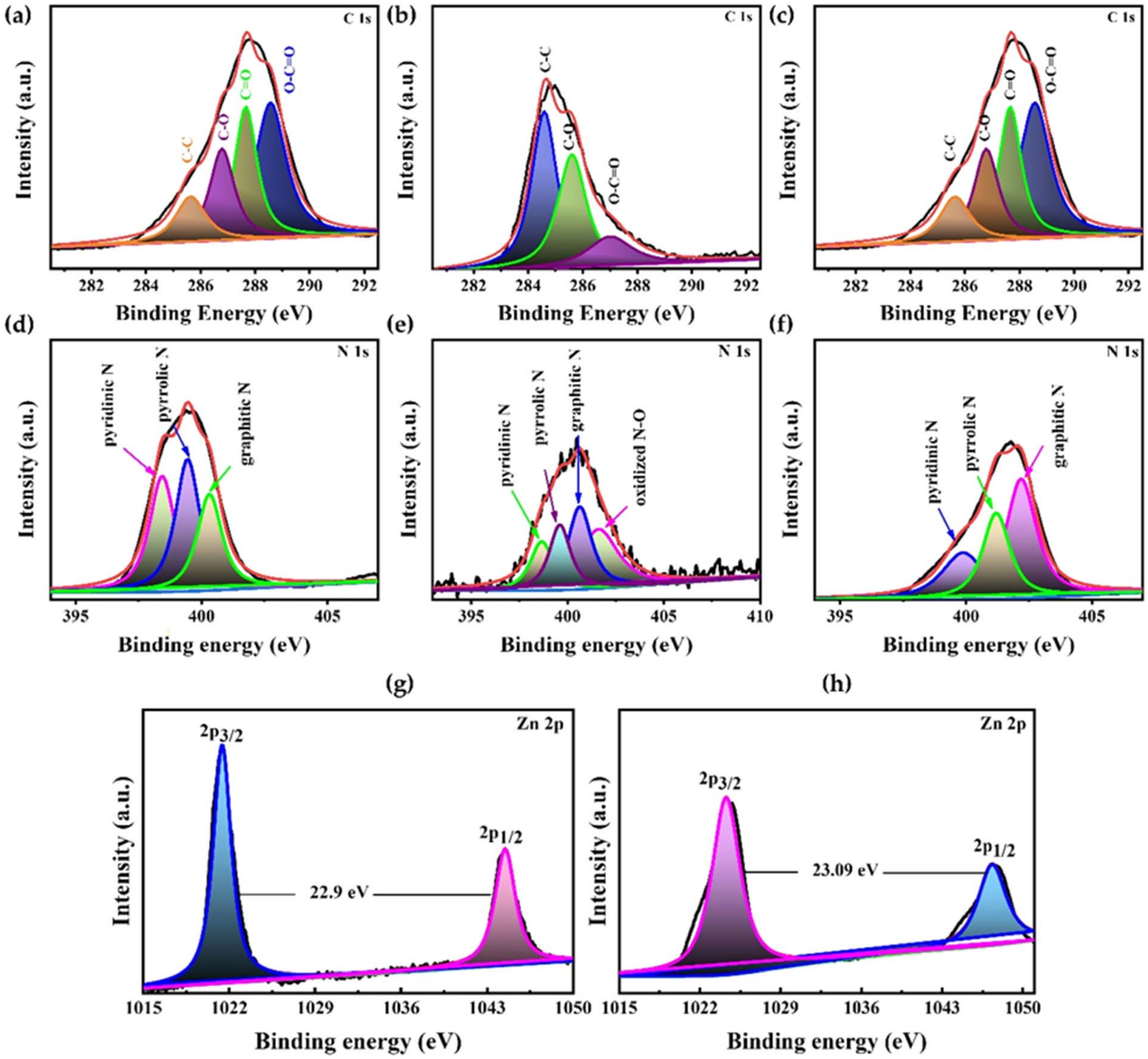

Fig. 3 High-resolution XPS spectra of pristine GO, ZIF-8 and the ZIF-8/GO composite: (a–c) C 1s and (d–f) N 1s spectra of GO, ZIF-8 and GO@ZIF-8, correspondingly; (g and h) Zn 2p spectra for ZIF-8 and GO@ZIF-8, correspondingly.

photocatalytic activity compared to the individual GO and ZIF-8 catalysts. This superior performance is likely due to the synergistic effects of the core–shell configuration, which improves the efficiency of the photocatalysis.

To quantify this performance, the degradation efficiency of the photocatalysts was calculated using the formula: $\eta(\%) = (C_{\text{o}} - C_t)/C_{\text{o}} \times 100$,[57] where C represents the initial concentration (at time $t = 0$), and C_t denotes the concentration at a given time t under visible light. Among the tested materials, the ZIF-8/GO composite demonstrated a notably high degradation efficiency for Rho-B, achieving 100% degradation within 100 min. This performance is significantly higher compared to GO (37.4%) and ZIF-8 (51.8%), as shown in Fig. 4(e).

Additionally, a linear kinetic relationship was assessed by fitting the degradation data to the pseudo-first-order model using the equation: $\ln(C_{\text{o}}/C_t) = -K_{\text{app}}t$.[58,59] Here, C_{o} represents the initial concentration of Rho-B, and C_t is the concentration at a specific time t. The linear fits of the data exhibited correlation coefficients (R^2) greater than 0.98, indicating a strong linear relationship. This suggests that the degradation of Rho-B adheres to pseudo-first-order reaction kinetics. The kinetic constant (k_{app}) for the degradation of Rho-B using the ZIF-8/GO catalyst was determined to be 0.0258 min^{-1}. This value is significantly higher than those for GO (0.0048 min^{-1}) and ZIF-8 (0.0074 min^{-1}), as depicted in Fig. 4(f). These findings underscore the superior catalytic efficiency of the ZIF-8/GO catalyst compared to the other tested materials.

The enhanced photocatalytic activity of the ZIF-8/GO catalyst can be attributed to several synergistic mechanisms: (1) the combination of ZIF-8 and GO results in an increased surface area and more active sites for the adsorption and degradation of pollutants like Rho-B, (2) ZIF-8 generates electron–hole pairs (e^-/h^+) under visible light, but these pairs tend to recombine, reducing efficiency and GO, acting as an excellent electron

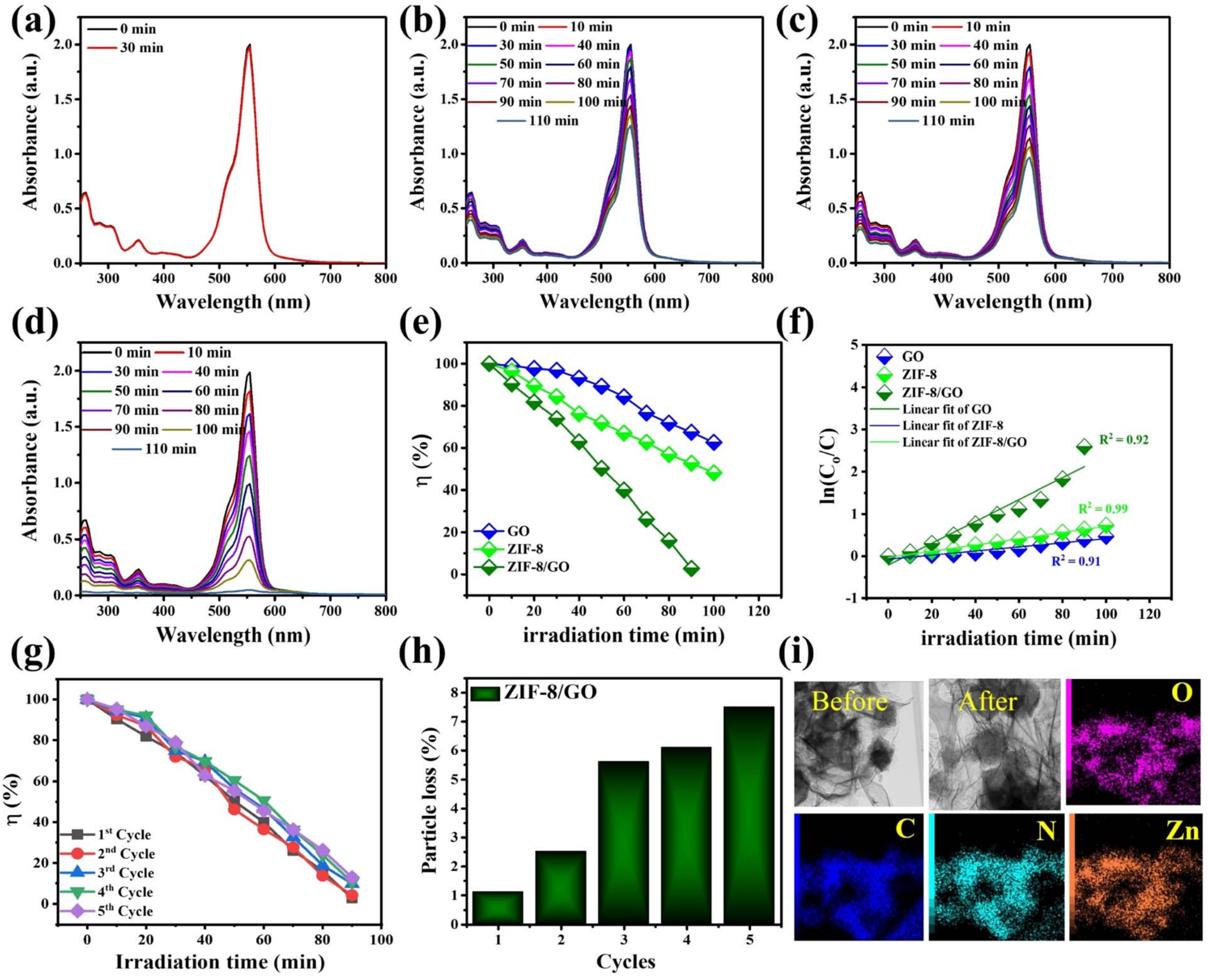

Fig. 4 Photocatalytic performance under visible light irradiation for approximately 100 min: (a) photolysis of Rho-B without the occurrence of photocatalysts, (b–d) time-dependent absorbance spectra of Rho-B in the presence of ZIF-8, GO, and ZIF-8/GO, respectively, (e and f) degradation efficiency and pseudo-1st-order fitted equations with respect to the visible time for ZIF-8, GO and ZIF-8/GO, (g) recycling runs of ZIF-8/GO catalyst towards the Rho-B degradation during the photocatalysis reaction, (h) weight loss against the runs during washing of the ZIF-8/GO and (i) TEM images before and after cycling the ZIF-8/GO with EDX mapping.

acceptor and transporter, captures and transports the photogenerated electrons from ZIF-8, thereby reducing recombination rates. This efficient charge separation and transfer mechanism allows more holes to remain available in ZIF-8 for the oxidation of pollutants, significantly enhancing the photocatalytic activity. Additionally, (3) the combination of ZIF-8 and GO broadens the light absorption spectrum, increasing the number of generated charge carriers. The configuration of ZIF-8/GO maximizes the contact area and ensures efficient electron transfer between the two materials, leading to improved photocatalytic performance.

In practical applications, the recyclability of a catalyst is a crucial indicator of its stability.[2] Therefore, the ZIF-8/GO catalyst was subjected to five successive photocatalytic cycles under consistent experimental conditions to evaluate its reusability. In each round, the optimized ZIF-8/GO material was applied to the degradation of Rho-B under visible light. Following each cycle, a 2 mL aliquot of the reaction mixture was taken, and the catalyst was separated from the Rho-B solution by centrifugation. The recovered catalyst was thoroughly rinsed with deionized water several times and then reused in the subsequent cycle under identical photocatalytic conditions. During the initial cycle, the ZIF-8/GO composite achieved complete degradation (100%) of Rho-B within 100 minutes of visible light exposure. For the subsequent cycles (second, third, fourth, and fifth), the degradation efficiencies were 95.7%, 90%, 89.3%, and 87.0%, respectively, as depicted in Fig. 4(g). Notably, even after five cycles, the degradation efficiency remained high at 87.0%, indicating that the ZIF-8/GO catalyst maintains substantial photocatalytic activity. The observed decrease in catalytic performance of approximately 13% in the fifth cycle is attributed to the loss of catalyst during the washing process.

The loss of photocatalyst during the experiments was calculated using the equation: $\eta(\%) = (W - W_t)/W \times 100$, where W is the initial mass of the catalyst and W_t is the remaining mass after use. After five consecutive photocatalytic cycles, the

ZIF-8/GO catalyst exhibited a suspension retention of only 12.8%, as shown in Fig. 4(h). This low value suggests that the photocatalytic process predominantly took place at the catalyst's surface rather than within the bulk liquid phase. To further assess the catalyst's durability, both its morphology and elemental composition were examined using transmission electron microscopy (TEM) before and after the reuse tests (Fig. 4(i)). TEM images revealed that the morphology of ZIF-8/GO remained intact even after five cycles, validating its structural stability. Additionally, EDX analysis was performed to validate the elemental composition after the stability evaluation. The analysis identified the occurrence of C 1s, O 1s, N 1s, and Zn 2p elements, as illustrated in Fig. 4(i). These results indicate that the structural morphology and the necessary elemental composition of the ZIF-8/GO were preserved before and after the stability test, confirming the robustness and stability of the structure.

3.3. Photodegradation of 5-Flu

Pharmaceutical contaminants, comprises 5-fluorouracil (5-Flu), stance is an important hazard to human health and environmental because of determination and potential for bioaccumulation. It is essential to employ an effective method for the degradation of these pollutants to mitigate their impact. Photocatalysis has arisen as an auspicious method, employing materials like GO and ZIF-8 to improve degradation efficiency under visible light. This study also examine alone photocatalytic capabilities of GO and ZIF-8 to establish a baseline comparison, with a specific focus on the degradation of 5-Flu.

Prior to the photocatalytic experiments, the degradation behavior of 5-FU under visible light irradiation without any catalyst was evaluated over a 30-minute period the corresponding absorbance spectrum is presented in Fig. 5(a). The results demonstrated that the absorbance of 5-Flu remained nearly unchanged throughout the exposure time, indicating that visible light alone was insufficient to induce photodegradation. Based on results, 5-Flu is stable and unaffected to breakdown by visible light alone, and a catalyst is necessary to facilitate its degradation.

Upon introducing photocatalysts such as GO, ZIF-8, and their composite, a notable enhancement in 5-Flu degradation under visible light was observed, emphasizing the photocatalytic potential of these materials. When GO was employed, the absorbance of 5-Flu gradually declined over a 100-minute irradiation period, as shown in Fig. 5(b). Significantly, the absorbance intensity of 5-Flu decreased more rapidly under similar time-frame, and corresponding results are shown in Fig. 5(c).

The use of ZIF-8/GO composite led to a significant decrease in the absorbance intensity of 5-Flu over 100-min visible light irradiation as depicted in Fig. 5(d). The optimal ZIF-8/GO photocatalyst demonstrated a remarkably high degradation efficiency for 5-Flu, achieving 97.4% degradation with a kinetic rate constant of 0.026 min^{-1}. This efficiency is significantly higher compared to GO (42.1%, 0.0057 min^{-1}) and ZIF-8 (67.7%, 0.011 min^{-1}), as the detailed calculated results at given interval of time are depicted in Fig. 5(e). This enhanced performance can be attributed to the synergistic effects of the core–shell structure, which boosts the overall efficiency of the photocatalysis.

The recyclability of ZIF-8/GO composite was also investigated through employing six consecutive photocatalytic cycles to assess its stability. After each cycle, 2 mL of the 5-Flu suspension was extracted and centrifuged to separate the solution from the catalyst, which was then washed and reused. The catalyst achieved 97.4% degradation of 5-Flu in the first cycle. Subsequent cycles showed degradation efficiencies of 96.2%, 94.5%, 93.3%, 91% and 88.2%, and the results are shown in Fig. S7. Despite a 12.8% decrease in efficiency by the six cycles, the ZIF-8/GO composite maintained high photocatalytic activity, with a final efficiency of 88.2%, indicating good stability and reusability.

3.4. Influence of the dosage amount and pH on Rho-B and 5-Flu degradation

To further investigate the impact of catalyst dosage on the degradation performance of Rho-B and 5-Flu, experiments were conducted using varying amounts of the ZIF-8/GO composite. Different dosages, specifically 0.25 g L^{-1}, 0.30 g L^{-1}, and 0.35 g L^{-1}, were tested to evaluate their effects on photocatalytic performance. For Rho-B, the degradation efficiencies observed were approximately 87.2%, 100%, and 76.9% at the dosages of 0.25 g L^{-1}, 0.30 g L^{-1}, and 0.35 g L^{-1}, respectively, as shown in Fig. 6(a). Similarly, for 5-Flu, varying the dosage of ZIF-8/GO affected the degradation rate. Further, the degradation efficiencies observed were approximately 87.6% at 0.25 g L^{-1}, 97.4% at 0.30 g L^{-1}, and 77.7% at 0.35 g L^{-1} of catalyst dosage, as illustrated in Fig. 6(b). The results indicate that the degradation efficiency of Rho-B and 5-Flu improved with increasing catalyst dosage up to an optimal level (0.30 g L^{-1}). However, further increases in dosage resulted in decreased efficiency, likely due to catalyst agglomeration or light scattering effects.

In addition, the impact of pH on the degradation of Rho-B and 5-Flu were conducted to assess how varying pH levels affect the photocatalytic efficiency of the ZIF-8/GO composite. Various experiments were collected in the range pH values, alkaline (pH 9), neutral (pH 7) and acidic (pH 3), to assess their effect on the degradation process. With Rho-B, the degradation efficiency varied with pH. Under an acidic environment (pH 3), the absorbance spectra of Rho-B showed moderate reduction after 100 min of visible light irradiation. In a neutral system (pH 7), the absorbance intensity decreased more significantly compared to the acidic condition. Overall, the ZIF-8/GO composite demonstrated good photocatalytic behavior in an alkaline medium with a pH of 9. The degradation efficiency of Rho-B was 47.3%, 64.8%, and 100% at pH values of 3, 7, and 9, when 100 min visible light exposed, respectively (Fig. 6(c)).

The highest degradation efficiency was achieved at alkaline pH (pH 9), where the catalyst performed optimally. At acidic pH (pH 3), efficiency decreased, likely due to increased protonation of the dye, which may hinder its interaction with the catalyst. *n* neutral conditions (pH 7), the degradation efficiency may have

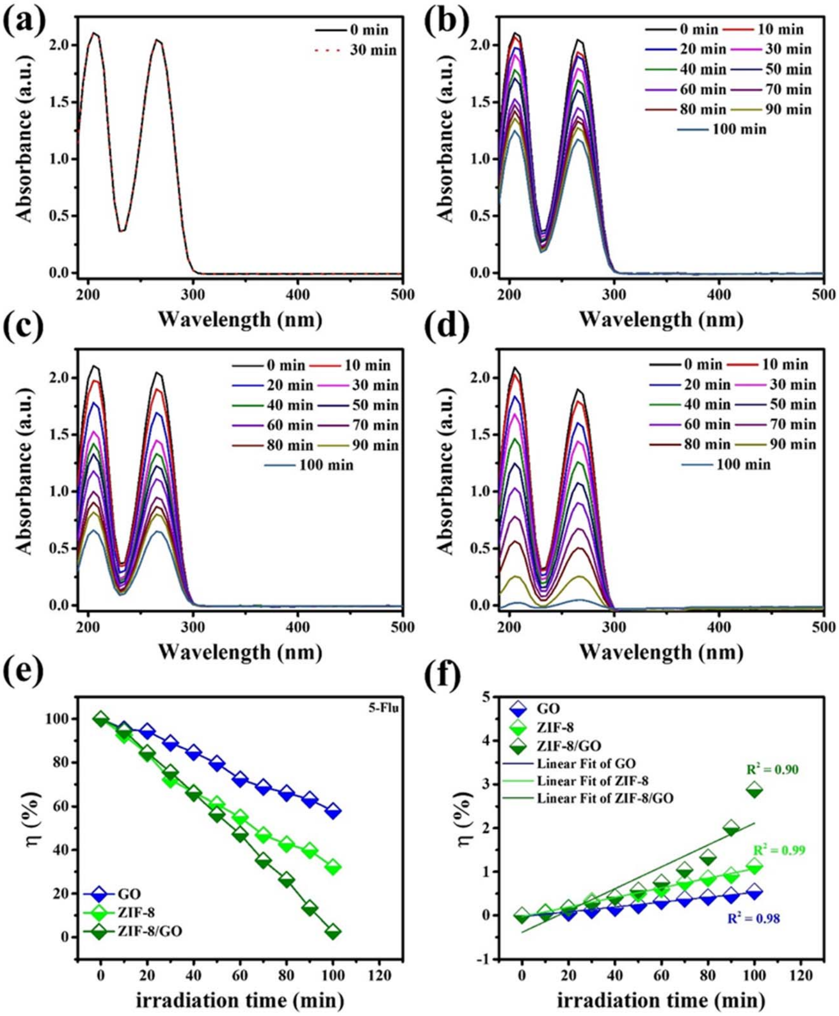

Fig. 5 Photocatalytic performance under visible light irradiation for approximately 100 min: (a) photolysis of 5-Flu without the occurrence of photocatalysts, (b–d) time-dependent absorbance spectra of 5-Flu in the occurrence of ZIF-8, GO and ZIF-8/GO at given interval of time and (e and f) degradation efficiency and pseudo-1st-order fitted equations with respect to the visible time for ZIF-8, GO and ZIF-8/GO.

reduced because of suboptimal conditions for the catalyst's reactivity. At neutral pH, the catalyst might not be in its most effective state for interacting with the dye, potentially resulting in less efficient degradation compared to the alkaline environment where the catalyst could be more reactive or better suited to the conditions.

For 5-Flu, the degradation efficiency was notably also influenced by pH. The highest performance was observed at neutral pH (pH 7, 97.4%, suggesting that the catalyst functions most effectively under these conditions. Degradation efficiency decreased at acidic pH (pH 3, 66.9%) and alkaline pH (pH 9, 76.9%), which could be due to changes in reactivity or stability of the catalyst at these pH levels. The corresponding results are shown in Fig. 6(d). The observed behavior can be attributed to the following factors: at lower pH levels, the primary active species, such as $^{\bullet}OH$ and $SO_4^{\bullet -}$, may react with excess h^+ ions to form less reactive substances (*e.g.*, H_2O and HSO_4^-). Conversely, at higher pH levels, some $SO_4^{\bullet -}$ may react with OH^-, producing $^{\bullet}OH$ with a relatively weaker oxidation potential. Therefore, a neutral pH environment is more suitable for the ZIF-8@GO catalyst, as it facilitates better degradation of 5-Flu under visible light, indicating its effective applicability in photocatalysis. These results indicate that the pH of the solution plays a crucial role in the photocatalytic degradation of both Rho-B and 5-Flu, with neutral conditions typically offering the most effective environment for optimal catalytic performance.

3.5. Mechanism study

To gain insight into the photocatalytic degradation mechanism of Rho-B using the ZIF-8/GO composite, a series of radical scavenging experiments were performed. These experiments aimed to identify the primary reactive species and clarify the role of photogenerated charge carriers involved in the degradation process. Various scavengers were introduced, including furfuryl alcohol (FFA) as a hydroxyl radical ($^{\bullet}OH$) scavenger, *p*-benzoquinone (*p*-BQ) for superoxide radicals ($^{\bullet}O_2^-$), potassium dichromate ($K_2Cr_2O_7$) for electrons (e^-), and EDTA-2Na for holes (h^+).[60,61] The results, presented in Fig. 7(a) and

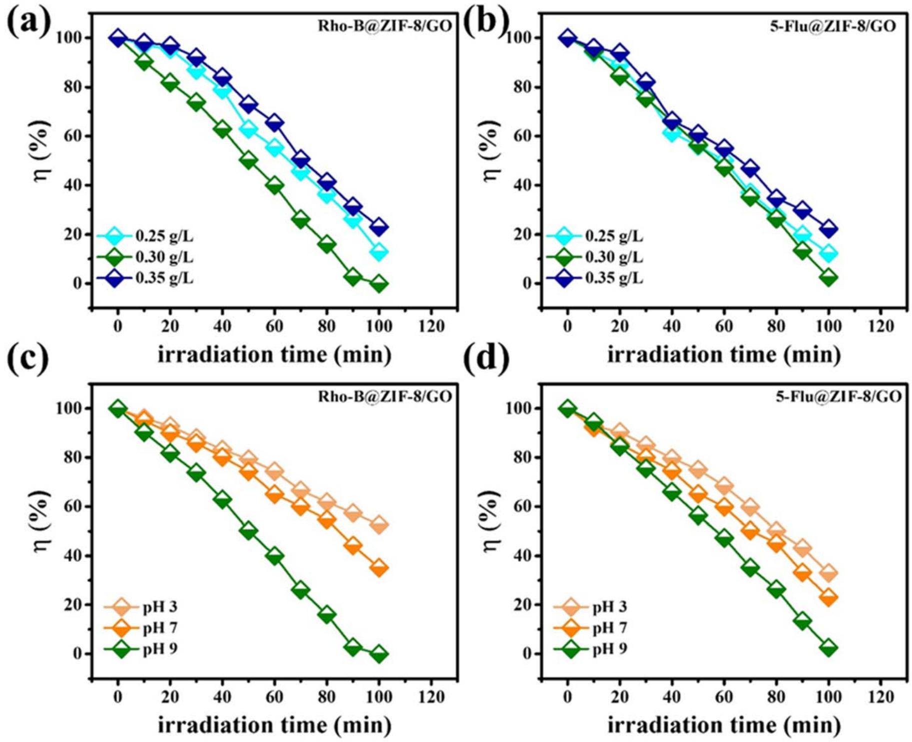

Fig. 6 Influence of the various operation conditions using the Rho-B and 5-Flu; (a and b) degradation efficiencies of Rho-B and 5-Flu in the occurrence of the ZIF-8/GO with respect of the irradiation time under visible light and such as 0.25, 0.30, 0.35 g L^{-1}, respectively, (c and d) degradation efficiency of Rho-B and 5-Flu in the presence of the ZIF-8/GO at various pH values including 3, 7 and 9.

supplementary Fig. S8–S11, show a marked decline in photocatalytic performance upon the introduction of FFA and *p*-BQ, indicating that $^{\bullet}OH$ and $^{\bullet}O_2^{-}$ are the primary reactive species responsible for dye degradation. In contrast, the addition of $K_2Cr_2O_7$ and EDTA-2Na led to only a slight reduction in activity, suggesting that although electrons and holes are generated, their direct involvement in pollutant breakdown is secondary to the ROS they help form. The degradation efficiencies of Rho-B in the presence of the scavengers followed the trend: $K_2Cr_2O_7$ (93.0%) > EDTA-2Na (86.01%) > *p*-BQ (39.2%) > FFA (34.5%).

Under light irradiation, ZIF-8 absorbs photons and generates electron–hole pairs (reaction 1). The photogenerated electrons are transferred to the GO sheets (reaction 2), where they interact with dissolved oxygen to yield superoxide radicals (reaction 3). These radicals can further react with water to produce hydroxyl radicals (reaction 4), both of which actively degrade the Rho-B molecules (reactions 5 and 6). Meanwhile, holes in ZIF-8 may contribute to oxidation processes, as supported by the moderate influence of EDTA-2Na. The following reactions summarize the mechanistic pathway:

$$\mathrm{ZIF-8 + hv \rightarrow ZIF-8\ [e^{-} + h^{+}]} \tag{1}$$

$$\mathrm{e^{-} + GO \rightarrow GO\ [e^{-}]} \tag{2}$$

$$\mathrm{GO\ [e^{-}] + O_2 \rightarrow {}^{\bullet}O_2^{-}} \tag{3}$$

$$\mathrm{{}^{\bullet}O_2^{-} + H_2O \rightarrow {}^{\bullet}OH + OH^{-}} \tag{4}$$

$$\mathrm{{}^{\bullet}OH + Rho\text{-}B \rightarrow [degraded\ products]} \tag{5}$$

$$\mathrm{O_2^{-} + Rho\text{-}B \rightarrow [degraded\ products]} \tag{6}$$

$$\mathrm{e^{-} + K_2Cr_2O_7 \rightarrow K_2Cr_2O_7\ [redox\ products]} \tag{7}$$

$$\mathrm{h^{+} + EDTA\text{-}2Na \rightarrow EDTA\text{-}2Na\ [oxidized\ specie]} \tag{8}$$

$$\mathrm{{}^{\bullet}OH + FFA \rightarrow FFA\ [oxidized]} \tag{9}$$

$$\mathrm{{}^{\bullet}O_2^{-} + \mathit{p}\text{-}BQ \rightarrow \mathit{p}\text{-}BQ\ [oxidized]} \tag{10}$$

The results highlight the synergistic role of the ZIF-8/GO composite in facilitating effective charge separation and promoting the generation of reactive oxygen species, leading to enhanced photocatalytic activity.

To validate the universality of this mechanism, analogous scavenger experiments were conducted using 5-fluorouracil (5-Flu) as the target pollutant under identical conditions. The observed trends closely mirrored those for Rho-B. Specifically, the addition of FFA and *p*-BQ significantly reduced degradation efficiency, confirming the central role of $^{\bullet}OH$ and $^{\bullet}O_2^{-}$ radicals. On the other hand, the effects of $K_2Cr_2O_7$ and EDTA-2Na were comparatively minor, reinforcing the idea that ROS, rather than the direct action of charge carriers, drive the photocatalytic reaction. Fig. 7(b) presents the comparative degradation efficiencies of 5-Flu under the influence of each scavenger, while detailed UV-vis spectral analyses are provided in Fig. S12(a–d), further supporting the proposed mechanism. These results

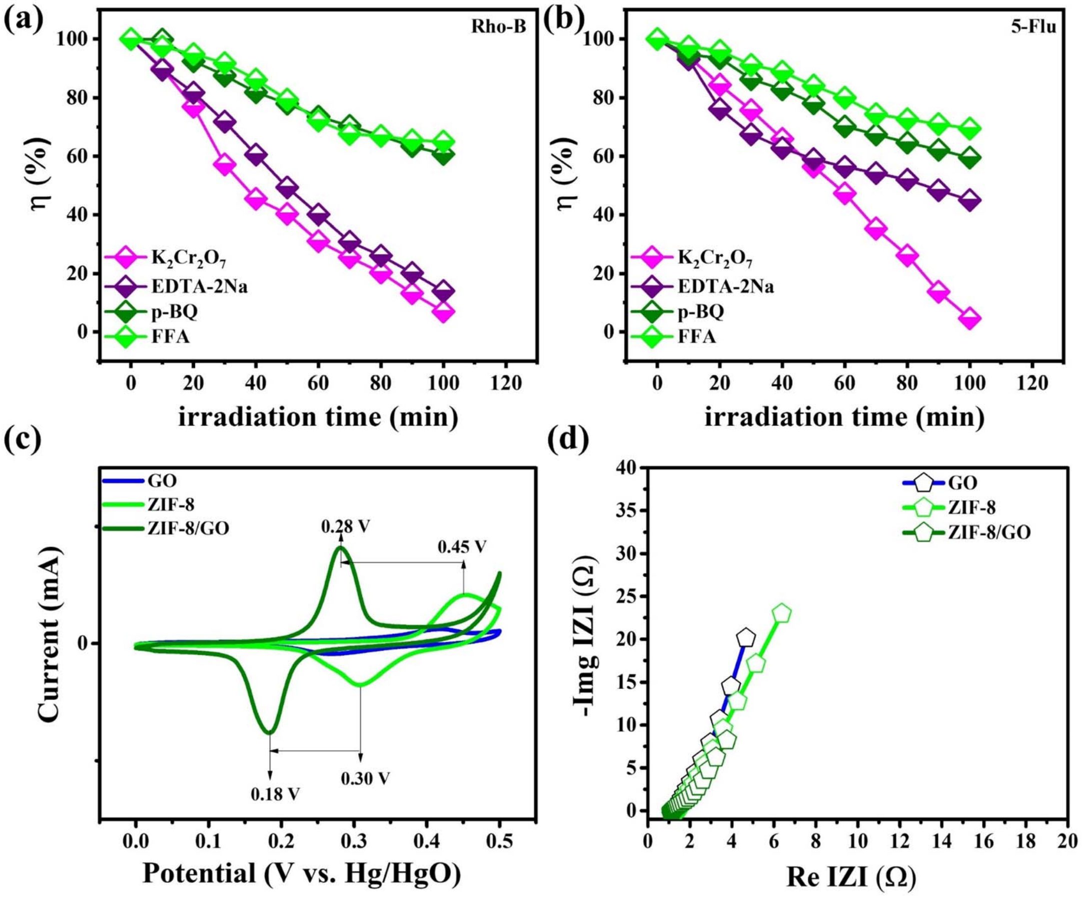

Fig. 7 Impacts of the scavengers including $K_2Cr_2O_7$, AO, *p*-BQ and FFA, respectively, on the photocatalytic degradation in the presence of ZIF-8/GO; (a) summary of the degradation efficiency of Rho-B with respect to the time, (b) summary of the degradation efficiency of 5-Flu with respect to the time, (c) CV profile for the ZIF-8, GO and their composite, and (d) Nyquist plot for the ZIF-8, GO and their composite.

demonstrate that the ZIF-8/GO composite effectively promotes charge separation and facilitates the formation of $^{\bullet}$OH and $^{\bullet}O_2{}^{-}$ radicals, which are the principal oxidants for both Rho-B and 5-Flu degradation. Overall, this study underscores the efficacy and versatility of the ZIF-8/GO photocatalyst in environmental remediation, showcasing its broad-spectrum capability in degrading structurally distinct organic pollutants *via* a unified ROS-driven mechanism.

The mechanism can also be rationalized through the band alignment of the ZIF-8/GO composite. Although we did not directly determine the band edges in this work due to the absence of the required facilities, the explanation can be constructed based on well-documented literature values. ZIF-8 is reported to possess a relatively wide bandgap of about 4.3–5.1 eV, with its conduction band positioned near −0.9 eV *versus* NHE, while GO exhibits a narrower effective bandgap of ∼2.9 eV and functions as an efficient electron acceptor owing to its conductive nature and favorable work function.[62–64] Upon visible-light excitation, electrons generated in the conduction band of ZIF-8 can readily migrate to the GO sheets, which not only prevents rapid recombination with holes but also facilitates the reduction of dissolved oxygen into $^{\bullet}O_2{}^{-}$ radicals. Meanwhile, the holes retained in the valence band of ZIF-8 participate in oxidation reactions, thereby sustaining the overall photocatalytic cycle.[65] This band alignment thus explains the improved charge separation and transfer dynamics, ultimately leading to the higher degradation efficiency observed in the ZIF-8/GO system, consistent with prior findings for similar MOF/GO photocatalysts.[66,67]

Photocatalysis includes the acceleration of a photoreaction in the existence of a catalyst.[68] Using this mechanism, the catalyst is generally a semiconductor material that, upon absorbing light, generates electron–hole pairs which can function chemical reactions. To further explore the photocatalytic activity mechanisms of the ZIF-8/GO composite, cyclic voltammetry (CV) and electrochemical impedance spectroscopy tests were conducted using a three-electrode setup in 3 M KOH aqueous electrolytes. The potential window range was applied from 0 to 0.5 V for CV analysis and EIS study was performed in the frequency range of 100 kHz–100 MHz. The CV electrochemical technique benefits to understand the redox method occurring on the surface of photocatalyst (ZIF-8/GO) and the contribution of numerous reactive species generated throughout the photocatalytic reaction. CV is a promising technique to probe the redox behavior of photocatalysts. As it includes sweeping the potential of an electrode engrossed in an electrolyte solution while measuring the resulting current. CV analysis of ZIF-8/GO demonstrates a well-defined redox peak and also express the excellent cycle stability, showed by overlapping traces (Fig. S13). The CV profile of ZIF-8/GO is consistent with our prior findings. As shown in figure, there are two distinct, reversible redox processes labeled reduction and oxidation for ZIF-8/GO, with the sharp increase at 0.5 V corresponding to the irreversible oxidation of water (Fig. 7(c)). Alone GO did not show any redox process, it suggests that its intrinsic photocatalytic activity is limited. This limitation can be attributed to several factors such as poor charge separation, low light absorption, and rapid recombination of photogenerated electron–hole pairs. The CV profile of alone GO is being consistent with the photodegradation of Rho-B and 5-Flu. The peak separations between the oxidation and the corresponding reduction are larger for ZIF-8 (0.15 V) compared to ZIF-8/GO (0.10 V), indicating that dye reduction occurs more slowly with ZIF-8 than with ZIF-8/GO. The faster dye reduction with ZIF-8/GO can be attributed to the following factors; (i) enhanced charge transfer: the presence of ZIF-8 in the composite may facilitate better charge transfer between GO and the Rho-B, leading to more efficient electron flow and faster reduction reactions, and (ii) improved surface interactions: the combination of ZIF-8 with GO could enhance the interaction between the ZIF-8/GO and the Rho-B, increasing the accessibility of Rho-B molecules to reactive sites on the surface of ZIF-8/GO. Moreover, at identical material loading, the ZIF-8/GO composite exhibits a significantly higher current density (5.9 mA), nearly doubling that of pure ZIF-8 (3.0 mA). This higher current density indicates that ZIF-8/GO exhibits superior catalytic activity compared to ZIF-8 and GO alone (1.0 mA).

The higher catalytic activity of ZIF-8/GO compared to ZIF-8 and GO alone, as reflected by the increased current density, can be attributed to several key factors. Firstly, the incorporation of GO into ZIF-8 significantly enhances the material's electronic conductivity. GO provides a conductive network that facilitates better electron transfer across the composite, thereby improving the overall catalytic performance. In addition, GO contributes additional active sites for catalytic reactions, which interact more effectively with reactants, further increasing the catalytic efficiency. The synergy between ZIF-8 and GO also results in optimized charge separation and reduced recombination of photogenerated electron–hole pairs, allowing more carriers to participate in catalytic processes. Moreover, the combination of ZIF-8 and GO may improve the surface properties of the material, such as its electronic structure and surface morphology, which enhances the interaction with reactants and boosts catalytic activity. However, the CV profile of ZIF-8/GO shows higher current density and smaller peak separations, suggesting that the improved photocatalytic performance is due to increased photocurrent and enhanced charge separation.

As shown in Fig. 7(d), the Nyquist plot reveals that ZIF-8/GO has a very low series resistance (R_s) of 1.4 Ω, compared to ZIF-8 (3.5 Ω) and GO (5.7 Ω). Notably, the charge transfer resistance (R_{ct}) for ZIF-8/GO is approximately 0.2 Ω, which is significantly lower than the R_{ct} values of 2.2 Ω for ZIF-8 and 4.1 Ω for GO. This suggests enhanced separation of photogenerated charges during the oxidation process and a higher density of active sites. The findings confirm that ZIF-8/GO facilitates more efficient charge transfer from the photocatalyst to the solution and exhibits lower charge transport resistance,[69,70] highlighting its enhanced photocatalytic activity.

4. Conclusions

In conclusion, the ZIF-8/GO composite demonstrates significant promise as an efficient photocatalyst for the removal of both pharmaceutical and organic contaminants from wastewater. The successful synthesis of the ZIF-8 nanocrystals on a GO matrix *via* an interfacial strategy result in a material with outstanding structural integrity well-defined morphological characteristics. The photocatalytic performance of this composite, evaluated through the degradation of Rho-B and 5-Flu under visible light, shows remarkable efficiencies of 100% and 97.4%, respectively, within 100 min. The photocatalyst's high efficiency is assigned to the synergistic interactions between ZIF-8 and GO, which enhance reactive site availability, contaminant diffusion, charge carrier separation, and light absorption. Furthermore, the ZIF-8/GO composite exhibits good recyclability, with only a modest decrease in degradation efficiency (12.8%) after five cycles, despite some material loss during the washing process. Overall, the study highlights the ZIF-8/GO photocatalyst as a highly effective and sustainable solution for wastewater treatment, addressing both pharmaceutical and organic pollutants with excellent efficiency and durability.

Author contributions

Iqra Ranani: funding acquisition, conceptualization, methodology, data curation, project administration, writing – original draft. Nguyen Tien Tran: formal analysis, investigation, writing – original draft. Muhammad Faheem Maqsood: formal analysis, investigation, visualization, writing – original draft. Karolien De Wael: investigation, visualization, writing – original draft. Mosab Kaseem: investigation, visualization, writing – original draft. Ghulam Dastgeer: investigation, visualization, writing – original draft. Hai Bang Truong: methodology, data curation, validation, supervision, project administration, writing – review & editing.

Conflicts of interest

There are no conflicts of interest to declare.

Data availability

. All data supporting the findings of this study are available within the paper and its SI. See DOI: **https://doi.org/10.1039/d5ra05177k**.

Acknowledgements

Dr Iqra Rabani would like to acknowledge the funding received from the European Union's Horizon 2020 research and innovation program, under the Marie Skłodowska-Curie grant agreement No. 101154941.

References

1 I. Rabani, R. Zafar, K. Subalakshmi, H.-S. Kim, C. Bathula and Y.-S. Seo, *J. Hazard. Mater.*, 2021, **407**, 124360.
2 I. Rabani, M. S. Tahir, W.-I. Lee, H. B. Truong, G. Dastgeer and Y.-S. Seo, *J. Cleaner Prod.*, 2023, **420**, 138324.
3 X. Li, H. Zhou, R. Qian, X. Zhang and L. Yu, *Chin. Chem. Lett.*, 2025, **36**, 110036.
4 I. Rabani, M. S. Tahir, F. Afzal, H. B. Truong, M. Kim and Y.-S. Seo, *J. Environ. Chem. Eng.*, 2023, **11**, 109235.
5 I. Rabani, H.-N. Jang, Y.-J. Park, M. S. Tahir, Y.-B. Lee, E.-Y. Moon, J. W. Song and Y.-S. Seo, *RSC Adv.*, 2022, **12**, 33653–33665.
6 B. T. Huy, X. C. Nguyen, V. K. H. Bui, N. N. Tri, I. Rabani, N. H. T. Tran, Q. V. Ly and H. B. Truong, *J. Environ. Sci.*, 2024, **144**, 212–224.
7 M. Zhou, H.-H. Wu, Y. Wu, H. Wang, X.-J. Liu, S.-H. Jiang, X.-B. Zhang and Z.-P. Lu, *Rare Met.*, 2024, **43**, 3370–3382.
8 I. Rabani, C. Bathula, R. Zafar, G. Z. Rabani, S. Hussain, S. A. Patil and Y. S. Seo, *J. Environ. Chem. Eng.*, 2021, **9**, 104852.
9 Y. Yang, Y. S. Ok, K.-H. Kim, E. E. Kwon and Y. F. Tsang, *Sci. Total Environ.*, 2017, **596**, 303–320.
10 I. Rabani, H. Park, G. Dastgeer, S. U. Khan, M. Altaf, Y. A. Kumar, M. Kim and Y.-S. Seo, *J. Photochem. Photobiol., A*, 2024, 115827.
11 M. Mišík, M. Filipic, A. Nersesyan, M. Kundi, M. Isidori and S. Knasmueller, *Water Res.*, 2019, **164**, 114953.
12 H.-J. Lee, K. Y. Kim, S.-Y. Hamm, M. Kim, H. K. Kim and J.-E. Oh, *Sci. Total Environ.*, 2019, **659**, 168–176.
13 M. Nkoom, G. Lu and J. Liu, *Environ. Sci.: Processes Impacts*, 2018, **20**, 1640–1648.
14 Z. Wang, X.-H. Zhang, Y. Huang and H. Wang, *Environ. Pollut.*, 2015, **204**, 223–232.
15 Z. Zhang, B. Wang, H. Yuan, R. Ma, J. Huang, S. Deng, Y. Wang and G. Yu, *Emerging Contam.*, 2016, **2**, 148–156.
16 V. Booker, C. Halsall, N. Llewellyn, A. Johnson and R. Williams, *Sci. Total Environ.*, 2014, **473**, 159–170.
17 J. Zhang, V. W. Chang, A. Giannis and J.-Y. Wang, *Sci. Total Environ.*, 2013, **445**, 281–298.
18 R. Guo, F. Zheng and J. Chen, *RSC Adv.*, 2015, **5**, 76772–76778.
19 R. Janssens, M. Cristovao, M. Bronze, J. Crespo, V. Pereira and P. Luis, *J. Environ. Chem. Eng.*, 2019, **7**, 103351.
20 J. M. Rosa, E. B. Tambourgi, R. M. Vanalle, F. M. C. Gamarra, J. C. C. Santana and M. C. Araújo, *J. Cleaner Prod.*, 2020, **246**, 119012.
21 H. Yu, D. Dou, X. Zhang, L. Zhang, H. Dong and H. Yu, *J. Cleaner Prod.*, 2020, **242**, 118548.
22 X. Wei, S. Shao, X. Ding, W. Jiao and Y. Liu, *J. Cleaner Prod.*, 2020, **248**, 119179.
23 L. Xu, X. Ma, J. Niu, J. Chen and C. Zhou, *J. Hazard. Mater.*, 2019, **379**, 120692.
24 Y. Wang, C. Zhou, J. Wu and J. Niu, *Chin. Chem. Lett.*, 2020, **31**, 2673–2677.
25 A. Fernandes, P. Makoś, Z. Wang and G. Boczkaj, *Chem. Eng. J.*, 2020, **391**, 123488.
26 A. Fernandes, M. Gągol, P. Makoś, J. A. Khan and G. Boczkaj, *Sep. Purif. Technol.*, 2019, **224**, 1–14.
27 K. Fedorov, M. Plata-Gryl, J. A. Khan and G. Boczkaj, *J. Hazard. Mater.*, 2020, **397**, 122804.
28 Q. Fang, Q. Sun, R. Zhong, H. Wang and J. Qi, *Mater. Today Chem.*, 2025, **46**, 102770.
29 K. Karuppasamy, I. Rabani, D. Vikraman, C. Bathula, J. Theerthagiri, R. Bose, C.-J. Yim, A. Kathalingam, Y.-S. Seo and H.-S. Kim, *Environ. Pollut.*, 2021, **272**, 116018.
30 I. Rabani, S.-H. Lee, H.-S. Kim, J. Yoo, S. Hussain, T. Maqbool and Y.-S. Seo, *J. Environ. Chem. Eng.*, 2021, **9**, 105845.
31 H. Guo, B. Wang, P. Hu and H. Wang, *J. Environ. Chem. Eng.*, 2025, **13**, 116417.
32 J. Guo, H. Shi, X. Huang, H. Shi and Z. An, *J. Colloid Interface Sci.*, 2018, **515**, 10–17.
33 N. Suzuki, T. Sanada, C. Terashima, T. Suzuki, T. Arai, S. Saitou, T. Kawashima, A. Mizutani, T. Saitou and K. Nakata, *J. Appl. Electrochem.*, 2017, **47**, 197–203.
34 I. Rabani, J.-W. Lee, S. R. Choi, J.-Y. Park, S. A. Patil, G. Turpu, M. Kim and Y. Soo-Seo, *J. Energy Storage*, 2023, **62**, 106885.
35 N. W. Ockwig, O. Delgado-Friedrichs, M. O'Keeffe and O. M. Yaghi, *Acc. Chem. Res.*, 2005, **38**, 176–182.
36 Y. Zhang, S. Yuan, X. Feng, H. Li, J. Zhou and B. Wang, *J. Am. Chem. Soc.*, 2016, **138**, 5785–5788.
37 H. Zheng, Y. Zhang, L. Liu, W. Wan, P. Guo, A. M. Nyström and X. Zou, *J. Am. Chem. Soc.*, 2016, **138**, 962–968.
38 W. Zhang, B. Zheng, W. Shi, X. Chen, Z. Xu, S. Li, Y. R. Chi, Y. Yang, J. Lu and W. Huang, *Adv. Mater.*, 2018, **30**, 1800643.
39 I. Rabani, J.-W. Lee, T. Lim, H. B. Truong, S. Nisar, S. Afzal and Y.-S. Seo, *RSC Adv.*, 2024, **14**, 118–130.
40 I. Rabani, M. S. Tahir, S. Nisar, M. Parrilla, H. B. Truong, M. Kim and Y.-S. Seo, *Electrochim. Acta*, 2024, **475**, 143532.
41 F. Cacho-Bailo, B. Seoane, C. Téllez and J. Coronas, *J. Membr. Sci.*, 2014, **464**, 119–126.
42 S. Gadipelli, W. Travis, W. Zhou and Z. Guo, *Energy Environ. Sci.*, 2014, **7**, 2232–2238.
43 H. Wu, W. Zhou and T. Yildirim, *J. Am. Chem. Soc.*, 2007, **129**, 5314–5315.
44 J. Qiu, X. Zhang, Y. Feng, X. Zhang, H. Wang and J. Yao, *Appl. Catal., B*, 2018, **231**, 317–342.
45 X. Xie, C. Mao, X. Liu, L. Tan, Z. Cui, X. Yang, S. Zhu, Z. Li, X. Yuan and Y. Zheng, *ACS Cent. Sci.*, 2018, **4**, 724–738.
46 T. Cai, L. Wang, Y. Liu, S. Zhang, W. Dong, H. Chen, X. Yi, J. Yuan, X. Xia and C. Liu, *Appl. Catal., B*, 2018, **239**, 545–554.
47 D. Asefi, N. M. Mahmoodi and M. Arami, *Colloids Surf., A*, 2010, **355**, 183–186.

48 S. A. Soomro, I. H. Gul, H. Naseer, S. Marwat and M. Mujahid, *Curr. Nanosci.*, 2019, **15**, 420–429.

49 M. Kruk and M. Jaroniec, *Chem. Mater.*, 2001, **13**, 3169–3183.

50 Z. Li, X. Huang, C. Sun, X. Chen, J. Hu, A. Stein and B. Tang, *J. Mater. Sci.*, 2017, **52**, 3979–3991.

51 R. S. Gohar, S. Manzoor, T. Munawar, S. Gouadria, M. F. Ashiq, F. Iqbal, F. Aftab, M. Najam-Ul-Haq, A. Trukhanov and M. N. Ashiq, *J. Energy Storage*, 2022, **52**, 104930.

52 S. Luanwuthi, A. Krittayavathananon, P. Srimuk and M. Sawangphruk, *RSC Adv.*, 2015, **5**, 46617–46623.

53 Y. Li, X. Cai, S. Chen, H. Zhang, K. H. Zhang, J. Hong, B. Chen, D. H. Kuo and W. Wang, *ChemSusChem*, 2018, **11**, 1040–1047.

54 J. Ran, H. Chen, S. Bi, Q. Guo, Z. Deng, G. Cai, D. Cheng, X. Tang and X. Wang, *Cellulose*, 2020, **27**, 10447–10459.

55 T. Liu, J. Huang, Z. Huang, Q. Luo, H. Wu, Y. Meng, C. He and H. Li, *Chem. Eng. J.*, 2024, **486**, 150209.

56 J. Huang, Z. Huang, T. Liu, Y. Wen, J. Yuan, S. Yang and H. Li, *Chin. Chem. Lett.*, 2025, **36**, 110179.

57 S. Sekar, I. Rabani, C. Bathula, S. Kumar, S. Govindaraju, K. Yun, Y.-S. Seo, D. Y. Kim and S. Lee, *Environ. Res.*, 2022, **205**, 112201.

58 H. B. Truong, I. Rabani, B. T. Huy, N. H. T. Tran and J. Hur, *Chem. Eng. J.*, 2023, **466**, 143178.

59 G. Turpu, P. Das, Y.-S. Seo, I. Rabani and S. S. K. Reddy, *J. Phys. Chem. Solids*, 2024, **184**, 111673.

60 R. R. Palem, C. Bathula, G. Shimoga, S.-H. Lee, A. A. Ghfar, S. Sekar, H.-S. Kim, Y.-S. Seo and I. Rabani, *Int. J. Biol. Macromol.*, 2023, **253**, 126948.

61 Y. Zhang, W. Li, Z. Hu, X. Jing and L. Yu, *Chin. Chem. Lett.*, 2024, **35**, 108938.

62 A. Baghban, S. Habibzadeh and F. Z. Ashtiani, *RSC Adv.*, 2020, **10**, 22929–22938.

63 A. Aboraia, A. Darwish, V. Polyakov, E. Erofeeva, V. Butova, H. Y. Zahran, A. F. Abd El-Rehim, H. Algarni, I. Yahia and A. V. Soldatov, *Opt. Mater.*, 2020, **100**, 109648.

64 N. Sharma, M. Arif, S. Monga, M. Shkir, Y. K. Mishra and A. Singh, *Appl. Surf. Sci.*, 2020, **513**, 145396.

65 D. Behera, P. Priyadarshini and K. Parida, *Dalton Trans.*, 2025, **54**, 2681–2708.

66 M. Atighi, G. Falahati, M. Hasanzadeh, N. Gholami, H. Ahmadi and M. Najafi, *New J. Chem.*, 2025, **49**, 10751–10765.

67 M. M. Kaid, O. Elbanna, S. El-Hakam, H. M. El-Kaderi and A. A. Ibrahim, *J. Photochem. Photobiol., A*, 2022, **430**, 114001.

68 Y. Wen, J. Huang, H. Liu, J. Li, T. Liu, A. S. Belousov, S. Yang and H. Li, *Chem. Eng. J.*, 2025, 163596.

69 Y. Zheng, Y. Liu, X. Guo, Z. Chen, W. Zhang, Y. Wang, X. Tang, Y. Zhang and Y. Zhao, *J. Mater. Sci. Technol.*, 2020, **41**, 117–126.

70 D. Liu, P. Zhu, L. Yin, X. Zhang, K. Zhu, J. Tan and R. Jin, *J. Solid State Chem.*, 2021, **301**, 122309.